https://doi.org/10.5194/egusphere-2026-4578
Preprint. Discussion started: 17 August 2026

Quantifying methane emissions by combining multi-instrument airborne observations with regional atmospheric transport modelling: application to Madrid waste sites

Christian Fruck[1,a], Sebastian Wolff[1], Sven Krautwurst[2], Christoph Kiemle[1], Mathieu Quatrevalet[1], Martin Wirth[1], Jakob Borchardt[2], Oke Huhs[2], Konstantin Gerilowski[2], Michał Gałkowski[3,4], Christoph Gerbig[3], John P. Burrows[2], Heinrich Bovensmann[2], and Andreas Fix[1]

[1]Deutsches Zentrum für Luft- und Raumfahrt, Institut für Physik der Atmosphäre, Oberpfaffenhofen, Germany
[2]University of Bremen, Institute of Environmental Physics, Bremen, Germany
[3]Department Biogeochemical Signals, Max Planck Institute for Biogeochemistry, Jena, Germany
[4]Faculty of Physics and Applied Computer Science, AGH University of Kraków, Kraków, Poland
[a]now at: European Southern Observatory (ESO), Garching, Bavaria, Germany

Correspondence: Sebastian Wolff (sebastian.wolff@dlr.de) and Andreas Fix (andreas.fix@dlr.de)

Abstract.

Regulating the emission of methane (CH_4) from anthropogenic sources plays an important role in global climate mitigation strategies. The waste sector is responsible for some of the strongest localized sources and therefore its control has the potential for high impact reduction measures.

As shown in a related preceding publication, airborne lidar and imaging spectrometer data provide reliable measurements of CH_4 columns and can be used to estimate CH_4 fluxes from sources such as landfills. However, incomplete knowledge of the transport of greenhouse gases from the source to the measurement point is one of the main sources of uncertainty in flux determination.

In this paper, we improve the accuracy over previous emission estimates by applying a new analysis method, based on high-resolution regional-scale weather simulations to describe the atmospheric transport. We use this model to perform a combined fit to the CH_4 measurements from airborne lidar and passive remote sensing, as well as in situ measurements. The key improvement over previous estimates comes from explicitly accounting for the complex, time-varying wind field on the measurement day, which caused significant CH_4 accumulation that biased earlier cross-sectional flux estimates.

This investigation focuses on two waste facilities close to Madrid, Spain, which were overflown by the German research aircraft HALO during a flight of the CoMet 2.0 Arctic mission. The estimated emission rates for the two sites were determined to be $4.0 \pm 1.2\,\mathrm{t\,h^{-1}}$ (Pinto landfill) and $4.7 \pm 0.7\,\mathrm{t\,h^{-1}}$ (Valdemingómez waste site).

https://doi.org/10.5194/egusphere-2026-4578
Preprint. Discussion started: 17 August 2026

1 Introduction

Methane (CH_4) is the second most important anthropogenic greenhouse gas after carbon dioxide. Because of its relatively short atmospheric lifetime of about 10 years, it is an attractive target for near-term climate mitigation efforts (IPCC, 2023; Global Methane Pledge, 2024; UNEP, 2025). Waste-related activities, such as landfilling, are a major CH_4 source, even in developed countries. On August 4, 2022, the imaging spectrometer MAMAP2DL (Krautwurst et al., 2025) and the CH_4 and CO_2 lidar CHARM-F (Amediek et al., 2017) were operated together for the first time on the German HALO research aircraft. Along with in situ instruments, they measured CH_4 plumes from waste facilities near Madrid, Spain, where satellite data had pinpointed large CH_4 anomalies (Tu et al., 2022). This flight was carried out to test all instruments prior to a transfer to Canada where the CoMet 2.0 (Carbon Dioxide and Methane) Arctic mission[1] took place.

The remote sensing instruments delivered vertical CH_4 column measurements along the flight track. One upstream flight leg and nine plume overflights, which were roughly perpendicular to the plumes and wind direction, were flown. Each of the ten legs was about 50 km long and centred around the plumes, and aimed at capturing background CH_4 on both sides of the plumes. The emissions were so strong that the CH_4 plume enhancements could be identified up to a distance of 30 km from the waste sites. Krautwurst et al. (2025) have previously used these measurements to assess the CH_4 fluxes by means of cross-sectional flux measurements that exploit the contrast between the plume enhancements and the background.

However, a major uncertainty of such an approach are variations of the plume enhancements due to wind shear and turbulence (Wolff et al., 2021). Cross-sectional flux measurements only deliver accurate emission rates under homogeneous and steady flow conditions. Often, as is the case here, these conditions are unknown due to a lack of wind measurements and/or not met due to complex flow. Variable wind fields can only be adequately taken into account using a transport model that is based on 4D meteorological fields. Any change in speed or direction in the wind field can lead to local accumulation or dilution of a trace gas that is emitted at a constant rate, resulting in significant emission uncertainties. In the present case, ERA5 reanalyses (Hersbach et al., 2023) indicate an increasing wind speed over the course of the measurements that were recorded during a time interval of about three hours. Furthermore, shortly before the measurements were taken, the wind direction changed by nearly 180 degrees. A close inspection of the data reveals that this direction change led to a residual accumulated CH_4 plume still originating from the waste sites, yet located over the city of Madrid (Krautwurst et al., 2025), as well as a CH_4 'puff' that formed over the sources during a phase of low wind speed and advected thereafter (see also Fig. 2). Without the transport model information these features could have been misinterpreted as originating from other sources. Those circumstances motivated us to test a novel flux calculation approach using a χ^2-fit-based inversion system, utilizing a high-resolution transport model (WRF Version 4.4.2 Skamarock et al., 2019) in a computationally cost-efficient way, similar to Ye et al. (2020).

Passive and active remote sensing from aircraft and satellites offers very promising perspectives to quantify greenhouse gas emissions both regionally and globally, yet lacks flow information. Thus, we are convinced that the efficient combination with a transport model will be of great value for monitoring, verification and mitigation actions foreseen in the Global Methane Pledge (2024) and the Climate and Clean Air Coalition (UNEP, 2025).

[1] CoMet 2.0 Arctic webpage, last access: June 3 2026

https://doi.org/10.5194/egusphere-2026-4578
Preprint. Discussion started: 17 August 2026

In this paper, we improve upon emission estimates from the Madrid waste sites previously obtained using the cross-sectional flux method (Krautwurst et al., 2025), who reported a combined emission rate of $\approx 13\,\mathrm{t\,h^{-1}}$ with uncertainties of 26 % to 38 %. The key improvement comes from taking into account the complex transport pattern that occurred on the measurement day due to spatiotemporal variability of the wind. Details on the instrumentation and the measurement conditions can be found in the preceding publication (Krautwurst et al., 2025). This work focuses on the new analysis approach (Sect. 2) and the resulting Madrid waste site $\mathrm{CH_4}$ fluxes (Sect. 3).

2 Methods and data

2.1 Measurements and instrumentation

The data discussed and analysed here were recorded during the CoMet 2.0 Arctic campaign, using a campaign-specific instrument suite on the German High Altitude and Long Range (HALO) research aircraft. The main target areas of the CoMet 2.0 campaign were the Canadian wetlands and permafrost regions, as well as fossil-fuel extraction sites. The measurements over the Madrid waste facility sites, the Mancomunidad del Sur landfill in the municipality Pinto (hereafter: Pinto landfill) and the Valdemingómez technology park (hereafter: Valdemingómez waste site), were part of a scientific test flight before the transfer to the campaign base in Canada. The technology park houses various waste facilities such as landfills (partly closed, partly still active, and partly equipped with a gas recovery system), and waste treatment and biomethane plants. For 2022, the year of the measurement flight, the Spanish Pollutant Release and Transfer Register (PRTR) reported annual $\mathrm{CH_4}$ emissions for both sites of $0.2\,\mathrm{t\,h^{-1}}$ (for further details on the waste treatment sites and their emissions, see Krautwurst et al., 2025, and references therein).

The decision to select this target for the test flight was prompted by reports of unexpectedly high methane emissions of around $8.8\,\mathrm{t\,h^{-1}}$ in 2021 from landfills in the Madrid area. This was reported in a web story by ESA (2021), based on measurements by GHGSat during two overflights. In addition, Tu et al. (2022) analysed Sentinel 5p observations over a period of almost 3 years and drew similar conclusions, estimating an emission rate from the region of about $7\,\mathrm{t\,h^{-1}}$. More recently, Domínguez-Sáez et al. (2026) combined continuous ground-based $\mathrm{CH_4}$ measurements with HYSPLIT dispersion modelling and reported episodic emission rates from the Pinto and Valdemingómez sites of up to 6–13 $\mathrm{t\,h^{-1}}$, occasionally several times higher than official inventory-based hourly means.

Remote-sensing measurements over the area were performed on August 4, 2022, between 11:00 and 12:30 UTC from a flight altitude of 8.3 km a.s.l., followed by a flight pattern within the boundary layer from around 12:45 to 13:30 UTC at an altitude of 2.3 km a.s.l or about 1.6 km a.g.l., well within the planetary boundary layer (PBL). The remote-sensing measurements were performed using the CHARM-F IPDA lidar (Amediek et al., 2017) and the MAMAP2DL imaging spectrometer (Krautwurst et al., 2025). While the lidar points to the nadir direction, the spectrometer has four independent along-track footprints (ground scenes) with a swath width of ≈ 3 km around the lidar nadir point. The in situ measurements were obtained with the Jena Instrument for Greenhouse gas measurements (JIG) that is based on a Cavity Ringdown Laser Spectrometer (CRDS) (Filges et al., 2015; Gałkowski et al., 2021).

https://doi.org/10.5194/egusphere-2026-4578
Preprint. Discussion started: 17 August 2026

During the remote-sensing measurement period the wind consistently came from approximately SSW, aligning the two waste facility areas in terms of wind direction. According to ERA5 reanalysis data, wind speeds ranged from 2 to $10\,\mathrm{m\,s^{-1}}$ throughout the boundary layer during this period. Cloud-free conditions prevailed throughout the entire flight over the targets, after which clouds gathered, which would have complicated interpretation of passive remote sensing observations significantly.

Table 1. Overview of the instrumental data used in this study.

Instrument	Technique	Measurement parameters[a]	Time	Flight level	Reference
CHARM-F	IPDA lidar	XCO_2 and XCH_4 with $\approx 800\,\mathrm{m}$ resolution along flight track	11:06–12:38 UTC	FL260 (8.3 km a.s.l.)	Amediek et al. (2017), Wolff et al. (2021)
MAMAP2DL	Imaging SWIR spectrometer	CO_2 and CH_4 **column anomalies**[b] binned to a swath of four independent $\approx 700 \times 700\,\mathrm{m}^2$ ground scenes	11:09–12:37 UTC	FL260 (8.3 km a.s.l.)	Krautwurst et al. (2025)
HALO-JIG	CRDS	Volume mixing ratios of CO_2, $\mathbf{CH_4}$, H_2O, CO	12:47–13:28 UTC	FL070 (2.3 km a.s.l.)	Filges et al. (2015), Gałkowski et al. (2021)
BAHAMAS	HALO basic data acquisition system	Wind, pressure, temperature, humidity, **aircraft attitude data**	Continuous	All	Giez et al. (2023)

[a] From the measurement parameters of the instruments only the ones given in **bold** are used in this study.
[b] During the retrieval process, MAMAP2DL's CH_4 column anomalies are normalised to the locally measured CH_4 background. This gives the additional CH_4 amount in the atmosphere due to an upwind emission source as a percentage of the local background column concentration in $\mathrm{molec\,cm^{-2}}$ (for details, see Krautwurst et al., 2025) .

2.2 Flux inversion scheme

In this analysis of the CoMet 2.0 Madrid dataset, we employ a flux inversion approach based on regional-scale weather simulations using the Weather Research and Forecast Model (WRF, Skamarock et al., 2019). A single χ^2 fit is used to minimise the difference between the measured CH_4 from CHARM-F, MAMAP2DL, and JIG and the simulated CH_4 by adjusting the scaling factors of each source. To determine the fluxes, we assign an individual tracer to each source in the WRF simulation. This enables the emission strength of each source to be scaled up or down in order to compute optimised CH_4 mole fractions as a function of space and time. In the initial phase of the analysis, we tried using several tracers for each of the two waste sites to account for small-scale spatial emission inhomogeneities. However, the fit results revealed that the dataset cannot constrain that higher spatial resolution. The three instruments used in this study rely on different measurement principles and therefore provide different measured quantities: CHARM-F yields XCH_4, MAMAP2DL provides total background-normalised CH_4 column anomalies (or just CH_4 column anomalies), and JIG measures in situ CH_4 volume mixing ratios (see Table 1). We

https://doi.org/10.5194/egusphere-2026-4578
Preprint. Discussion started: 17 August 2026

thus derive instrument-specific simulated quantities from the modelled CH_4 mole fractions, corresponding to each of these observed quantities.

In our flux optimisation scheme, we make two assumptions: first, that the sinks of CH_4 are negligible; and second, that each tracer from the various sources behave as linearly scaling quantities. This means that the total mole fraction at each grid point is the sum of all individual tracer CH_4 values associated with different sources. This allows us to apply individual, source-specific scaling factors to these tracers before adding them together. In more formal terms:

$$R(\mathbf{r},t) = \sum_{j=1}^{N} S_j \cdot \underline{R}_j(\mathbf{r},t). \tag{1}$$

$R(\mathbf{r},t)$ is the modelled total mole fraction of the trace gas as function of space $\mathbf{r}$ and time t. $\underline{R}_j(\mathbf{r},t)$ is the mole fraction of tracer j obtained from the simulation. The S_j are the scaling factors adjusted in the fit, each controlling the emission strength of one source and thus its contribution to the total mole fraction. The model uses one tracer for each of the two waste sites and a background component, which is based on the Copernicus Atmosphere Monitoring Service (CAMS) global data assimilation model (CAMS, 2023). Other anthropogenic CH_4 emissions within the domain, prescribed from the EDGAR v8.0 inventory (Crippa et al., 2023, see also Sect. 2.3), are included as a fixed tracer but not optimised in the fit, as their contribution is several orders of magnitude smaller than the landfill signals and has a negligible effect on the fit results.

The 4-dimensional data is condensed to simulated values along the flight track by integrating the vertical, and linearly interpolating the other grid dimensions. Shortly before the measurements, the wind field over the study area underwent a rotation. The exact timing and dynamics of this rotation define the position and shape of the residual CH_4 plume. While the model captures the rotation, the timing is off by a mostly constant factor. To account for this mismatch, we introduced a temporal offset as an additional fit parameter, which allows sampling the model field at a shifted stage of the simulated flow, thereby compensating for the timing discrepancy between model and observations (see also Fig. 2 and the video supplement; Fruck and Wolff, 2026). An offset to the column anomaly needs to be added as a fit parameter. This offset is calculated with respect to a subset of the observations which represents the CH_4 background. The full list of fit parameters with their corresponding allowed parameter ranges is shown in Table 2.

Table 2. Fit parameters and their allowed ranges.

Parameter		Allowed range
Time shift (model vs. data)	Δt	$\pm 5000\,\mathrm{s}$
CAMS background scaling factor	S_{CAMS}	$0.9 \ldots 1.1$
In situ background scaling factor	S_{IS}	$0.9 \ldots 1.1$
Column anomaly offset	δ_{CA}	$-1\,\% \ldots 1\,\%$
Pinto emission scaling factor	S_{Pinto}	$0.1 \ldots 10$
Valdemingómez emission scaling factor	S_{Valde}	$0.1 \ldots 10$

https://doi.org/10.5194/egusphere-2026-4578
Preprint. Discussion started: 17 August 2026

Figure 1. Illustration of the size and location of the domains used in the WRF setup.

Base map data © OpenStreetMap contributors, distributed under the Open Data Commons Open Database License (ODbL) 1.0.

2.3 Simulation setup

For modelling the transport of CH_4 emitted by the two Madrid waste sites, we use the WRF Greenhouse Gas Model (WRF-GHG, Beck et al., 2011), a passive tracer transport module coupled to WRF version 4.4.2 (Skamarock et al., 2019). A passive

https://doi.org/10.5194/egusphere-2026-4578
Preprint. Discussion started: 17 August 2026

tracer is transported by the model without any chemical loss or production, i.e. all CH_4 sinks, including reactions with OH and Cl radicals, photochemistry, and soil deposition, are assumed negligible.

The simulation setup includes two nested domains, with the central coordinate of the Valdemingómez waste site (40.332°N, 3.580°W) serving as the centre for both domains (see Fig. 1). The simulations are performed as two-way nested runs, meaning that feedback between the outer and inner domains is enabled in both directions. The domain configurations are detailed in Table 3, with the inner domain having a horizontal resolution of $1\,\mathrm{km}$, a WRF-internal calculation interval of $6\,\mathrm{s}$, and a history interval of $5\,\mathrm{min}$, representing the temporal resolution of the simulation output files.

Table 3. WRF domains.

Parameter	Outer domain	Inner domain
Number of horiz. grid cells	280×280	280×280
Size of horiz. grid cells	$5\,\mathrm{km}$	$1\,\mathrm{km}$
Number of vert. levels	57	57
Model top	$200\,\mathrm{hPa}$	$200\,\mathrm{hPa}$
Calculation interval	$30\,\mathrm{s}$	$6\,\mathrm{s}$
History interval	$5\,\mathrm{min}$	$5\,\mathrm{min}$

The meteorological data used for the initial and boundary conditions, as well as for grid-nudging in the outer domain, is ERA5 data (Hersbach et al., 2023), which is comprehensively described in Hersbach et al. (2020). CH_4 boundary conditions are provided by CAMS (2023). Background CH_4 emissions from anthropogenic sources other than the two waste sites are prescribed using the EDGAR v8.0 inventory for the year 2022 (Crippa et al., 2023). As initial-guess emission rates for the flux inversion scheme (see Sect. 2.2) we assume $5.0\,\mathrm{t\,h^{-1}}$ for Valdemingómez and $3.8\,\mathrm{t\,h^{-1}}$ for Pinto, as estimated from GHGSat high-resolution emission quantification, following hotspot identification with the Copernicus Sentinel-5P (ESA, 2021). We evenly distributed these emission rates over the grid cells occupied by parts of the waste sites, based on satellite imagery (Krautwurst et al., 2025, see Fig. 5 therein).

The overflight time was between 13:00 and 15:40 local time (11:00 to 13:40 UTC) on August 4, 2022. With the simulation initiated at 00:00 UTC on August 3, 2022, this results in a spin-up of $35\,\mathrm{h}$, sufficient for the model dynamics and boundary layer to reach a stationary state.

The measurements were carried out within 30 km from the CH_4 emission source. This means that the immediate turbulent transport after emission is relevant and that the measured plume is completely confined within the boundary layer. Previous studies have addressed the optimal WRF physics parametrisation configuration, without a clear best option emerging (Yver et al., 2013; Lauvaux and Davis, 2014; Lucas et al., 2017; Díaz-Isaac et al., 2019). The performance depends on climatic zone, season, synoptic situation and diagnostic variable considered (Banks et al., 2016; Gunwani and Mohan, 2017).

In order to assess the boundary layer turbulent transport uncertainties, simulations were carried out with different physics parametrisation options. The intention is not to perform a full transport uncertainty analysis of the model, as this would be

https://doi.org/10.5194/egusphere-2026-4578
Preprint. Discussion started: 17 August 2026

Table 4. WRF configuration

	Setting	Reference
WRF version	4.4.2	Skamarock et al. (2019)
Meteorological data	ERA5	Hersbach et al. (2023)
CH_4 mole fractions	CAMS v22r2	CAMS (2023)
CH_4 backgr. emis.	EDGAR v8.0	Crippa et al. (2023)
Spin-up	35 h	
Simulation start	2022-08-03 00:00	

beyond the scope of this paper, but rather to provide an estimate of the model output variations with different PBL schemes. For this, we choose five PBL schemes that are commonly used and have been shown to perform reliably in similar contexts (see also Table 5):

- Yonsei University Scheme (YSU, Hong et al. (2006)): A nonlocal K-profile scheme with explicit treatment of the entrainment layer, widely used for its robustness in representing boundary layer mixing and handling surface winds in complex terrain.
- Mellor–Yamada Nakanishi Niino Level 2.5 (MYNN2, Nakanishi and Niino (2009)): An improved turbulence closure model that predicts sub-grid scale turbulence kinetic energy (TKE), incorporating buoyancy effects and better representing vertical mixing and turbulence in both stable and convective boundary layers.
- Shin-Hong Scale–Aware Scheme (Shin-Hong, Shin and Hong (2015)): A scale-aware scheme for vertical transport in the convective boundary layer, with TKE and mixing length diagnostics. Vertical mixing in the stable PBL and free atmosphere follows YSU.
- Mellor–Yamada–Janjic Scheme (MYJ, Janjić (1994)): A local TKE-based scheme focused on simulating turbulence and mechanical mixing in stable boundary layers.
- University of Washington TKE Boundary Layer Scheme (UW, Bretherton and Park (2009)): A TKE-based scheme that handles both dry convective and marine boundary layers, suitable for various boundary layer conditions.

The surface layer scheme must be compatible with the chosen PBL scheme. Depending on the PBL scheme, we employ either the Revised MM5 Scheme ($sf\_sfclay\_physics = 1$, Jiménez et al., 2012) or the Eta Similarity Scheme ($sf\_sfclay\_physics = 2$, Janjić, 1994) (see Table 5). Further parametrisation options are listed in Appendix A.

https://doi.org/10.5194/egusphere-2026-4578
Preprint. Discussion started: 17 August 2026

Table 5. PBL scheme overview

PBL scheme	Abbreviation		Reference	Surface layer scheme	
Yonsei University Scheme	YSU	(1)	Hong et al. (2006)	Revised MM5	(1)
Mellor–Yamada Nakanishi Niino Level 2.5	MYNN2	(5)	Nakanishi and Niino (2009)	Revised MM5	(1)
Shin-Hong Scale–Aware Scheme	Shin-Hong	(11)	Shin and Hong (2015)	Revised MM5	(1)
Mellor–Yamada–Janjic Scheme	MYJ	(2)	Janjić (1994)	Eta Similarity	(2)
University of Washington TKE Scheme	UW	(9)	Bretherton and Park (2009)	Eta Similarity	(2)

Note that the surface layer scheme must be compatible with the chosen PBL scheme. Depending on the PBL scheme, we employed either the Revised MM5 Scheme (Jiménez et al., 2012) or the Eta Similarity Scheme (Janjić, 1994). The namelist options *bl_pbl_physics* for PBL scheme and *sf_sfclay_physics* for surface layer scheme are given in brackets.

2.4 Modelled observations

The data analysed for this study (XCH_4 from CHARM-F, column anomaly from MAMAP2DL, and in situ volume mixing ratio from JIG) are independent of each other and use very different observational techniques. For model-data comparison, the observations need to be modelled by sampling the 4D concentration fields, according to the measurement method.

CHARM-F XCH_4 model estimates are derived by averaging the modelled mole fractions $R_{\mathrm{CH_4},i}$ within the relevant grid cells (in the vertical direction), weighted according to layer thickness Δh_i, number density of air molecules $n_{\mathrm{air},i}$ and instrumental weighting function W_i (Ehret et al., 2008; Amediek et al., 2017):

$$\mathrm{XCH_4} = \frac{\sum_{i=1}^{N_{\mathrm{flh}}} R_{\mathrm{CH_4},i} \cdot \Delta h_i \cdot n_{\mathrm{air},i} \cdot W_i}{\sum_{i=1}^{N_{\mathrm{flh}}} \Delta h_i \cdot n_{\mathrm{air},i} \cdot W_i}. \tag{2}$$

Simulated MAMAP2DL column anomalies are calculated as the relative enhancement in total CH_4 column caused by the source components above the CAMS background, expressed as a percentage. As the WRF simulation only covers the atmospheric column up to an altitude of about 12 km, the column above the aircraft has to be accounted for separately. This is achieved by calculating the total column anomaly as the average value of anomaly of the partial column below flight altitude and zero as the anomaly of the partial column above. The computation of this average uses the column integrated number density of air molecules as weights.

$$\alpha_{\mathrm{CH_4}} = \frac{\sum_{i=1}^{N_{\mathrm{flh}}} \frac{R_{\mathrm{CH_4,src},i}}{R_{\mathrm{CH_4,bkg},i}} \cdot \Delta h_i \cdot n_{\mathrm{air},i}}{\sum_{i=1}^{N_{\mathrm{flh}}} \Delta h_i \cdot n_{\mathrm{air},i}} \cdot \frac{P_{\mathrm{sfc}} - P_{\mathrm{flh}}}{P_{\mathrm{sfc}}}. \tag{3}$$

$R_{\mathrm{CH_4,src},i}$ and $R_{\mathrm{CH_4,bkg},i}$ are the contributions to the CH_4 number concentration by tracers that originate from the two waste site sources and the background component from CAMS, respectively. The ratio of these components represents the relative CH_4 column anomaly. P_{sfc} and P_{flh} are the air pressures at ground and at flight altitude, and used as proxy for column integrated number density of air molecules. The second factor extrapolates the column anomaly measured in the column below the aircraft to the total column, under the assumption that the anomaly above the aircraft is zero, as described above.

Simulated JIG in situ values can in principle be derived more directly from the WRF simulation, by reading the simulated CH_4 mole fraction of the grid-cell containing the coordinates of the aircraft in space and time. In practice, however, it was

https://doi.org/10.5194/egusphere-2026-4578
Preprint. Discussion started: 17 August 2026

found that averaging the $2k+1$ adjacent z-layers (k layers below and above flight altitude) results in a much better agreement between measurements and simulation. Due to the vertical grid stretching of the WRF model, this corresponds to an asymmetric height range of approximately $-700\,\mathrm{m}$ to $+800\,\mathrm{m}$ around the flight altitude of $2.3\,\mathrm{km}$.

$$\overline{R}_{\mathrm{CH_4}} = \frac{\sum_{i=N_{\mathrm{flh}}-k}^{N_{\mathrm{flh}}+k} R_{\mathrm{CH_4},\,i} \cdot \Delta h_i \cdot n_{\mathrm{air},\,i}}{\sum_{i=N_{\mathrm{flh}}-k}^{N_{\mathrm{flh}}+k} \Delta h_i \cdot n_{\mathrm{air},\,i}}. \tag{4}$$

$\overline{R}_{\mathrm{CH_4}}$ is the local average that is used for the fit to the JIG observations.

2.5 Fitting procedure

We scale the source emission rates as fit parameters to minimise the difference between simulated and observed CH_4 using a χ^2 framework. For the χ^2-minimisation procedure we use the MINUIT algorithm (James and Roos, 1975), which is conveniently available via a Python wrapper in the form of *iminuit* (Dembinski et al., 2020).

Apart from the parameters that are of main scientific interest for this study, namely the flux scaling of the tracers injected at the location of the two waste sites (Pinto and Valdemingómez), a couple of additional parameters are not constrained and are left free for the optimisation to adjust (see also Table 2). Those parameters are:

- a background scaling that adjusts the CAMS-based concentration component,
- an offset to the MAMAP2DL column anomaly,
- an offset between the in situ and remote sensing background components and, finally,
- a time shift, allowing the model to be evaluated at earlier or later times with respect to the observations.

2.6 Uncertainty estimation

Even with this more sophisticated approach, compared to simpler cross-sectional flux evaluation methods, the main source of uncertainties on the fluxes is still to be attributed to errors in the transport and its representation in the model. This becomes obvious when comparing WRF results obtained with different PBL-physics schemes.

Measurement uncertainties of the three instruments are propagated into the fit and are used for computing the curvature of the χ^2-parabola near its minimum. This curvature provides an estimate of the parameter uncertainties (Bevington and Robinson, 2003). However, the uncertainty contribution of the turbulent transport is not contained in this estimate and cannot easily be incorporated within a χ^2 or likelihood framework. Therefore, we use a conservative approach to quantify this dominant source of flux uncertainties: Similar to Ye et al. (2020), we use the scatter between the five different WRF PBL-physics fit results as a proxy for the turbulent transport uncertainty. We ignore the fact that some of the simulation runs produce results that more closely resemble our data after fitting than others (see Tab. C1). We use the standard deviation of the flux estimates from the different runs as proxy for the uncertainty in the transport modeling.

https://doi.org/10.5194/egusphere-2026-4578
Preprint. Discussion started: 17 August 2026

3 Results

The fitted model CH_4 fields reproduce the key structures present in the observations. As an illustration, Figure 2 shows a snapshot of the column CH_4 mole fractions over the study area. The main features are: (i) a plume whose position changed following a clockwise rotation of the wind field, appearing north-east of the waste sites at the time of the measurements (due to the wind direction being aligned with both sources at that time, just a single plume containing both emissions is visible), (ii) a CH_4 puff that accumulated during a period of very low wind speeds, and (iii) a residual plume over the city of Madrid formed by the conditions before the rotation.

Figure 3 shows a comparison of the measured time series from CHARM-F, MAMAP2DL and JIG (i.e. CH_4 column, column anomaly, and concentration, respectively). The observations are shown together with the best-fit results obtained from the five WRF runs with different PBL-physics schemes. All five fitted model time series capture the main features present in the observations, with larger differences appearing at finer detail. In particular, narrow enhancements in the measurements tend to be smoothed in the model, more than would be expected from the grid resolution and the data binning alone. Nevertheless, the fitted results consistently reproduce the characteristic pattern of a single plume downwind of the two waste sites, as well as a residual plume over the city of Madrid (Fig. 2). None of the PBL schemes shows an outlier behaviour. The residual scatter in the CHARM-F and MAMAP2DL measurements is mainly due to instrument noise. In case of MAMAP2DL all four ground traces along the swath are superimposed for the plot. The light blue peaks in this panel indicate that one or two ground traces occasionally were very close to the sources.

Table 6 shows the best-fit parameter results, averaged between different WRF runs, and their scatter, in terms of standard deviation between different WRF runs with varying PBL-physics schemes. Using this analysis scheme, we obtain the CH_4 emission rates from the Pinto and Valdemingómez waste sites as 4.0 and 4.7 $\mathrm{t\,h^{-1}}$, with uncertainty ranges of $\pm$ 31 % and $\pm$ 15 %, respectively. The combined emission rate from both sites is 8.7 $\mathrm{t\,h^{-1}}$, with an uncertainty range of $\pm$ 18 %. The uncertainties are dominated by transport model errors as seen in the discrepancies between individual WRF runs that use different PBL-physics schemes. These discrepancies far exceed the error estimate resulting from the propagation of measurement uncertainties through the fit (see Tab. C1).

The results presented in this work can be compared to those from the preceding analysis by Krautwurst et al. (2025), who used the cross-sectional flux method and found total emission rates of 12.1 and 13.3 $\mathrm{t\,h^{-1}}$ for the MAMAP2DL and CHARM-F instruments, respectively. Those numbers are substantially higher, yet the authors note that the CH_4 accumulation, predicted by the model and clearly seen in Fig. 2 (ii), could have had a significant impact on two out of the ten flight legs. Excluding these two legs from the analysis of Krautwurst et al. (2025) results in a lower emission rate of 9.6 $\mathrm{t\,h^{-1}}$, which is much closer to the figure reported here and within the uncertainty of this study (see Table 6). We finally note that the emission rates estimated by Krautwurst et al. (2025) of the Pinto landfill alone (4.2 and 5.2 $\mathrm{t\,h^{-1}}$ retrieved from MAMAP2DL and CHARM-F data, respectively), where measurements were not influenced by prior accumulation, yield results very comparable to our study (4.0 $\mathrm{t\,h^{-1}}$).

https://doi.org/10.5194/egusphere-2026-4578
Preprint. Discussion started: 17 August 2026

Table 6. Final averaged parameter[1] results and derived emission rates ($F_{\mathrm{Pinto/Valde/Total}}$) of the combined analysis, fitting all five PBL-physics schemes to the set of all three methane measurements. Uncertainties have been estimated as described in Section 2.6.

Parameter	Average result	Std. dev.	Uncert. [%]
F_{Pinto} [t h^{-1}]	**4.009**	**1.231**	**31**
F_{Valde} [t h^{-1}]	**4.656**	**0.692**	**15**
F_{Total} [t h^{-1}]	**8.665**	**1.519**	**18**
Δt [s]	-3177	368	11
S_{CAMS}	0.989	3×10^{-4}	0.03
S_{IS}	0.997	4×10^{-4}	0.04
δ_{CA} [%]	-0.296	0.038	13
S_{Pinto}	1.002	0.31	31
S_{Valde}	0.931	0.14	15
$F_{\mathrm{Pinto,CF}}$ [t h^{-1}]	4.2 / 5.2	-	38 / 37
$F_{\mathrm{Total,CF}}$ [t h^{-1}]	12.1 / 13.3 (9.6)[2]	-	27 / 26

[1] For a definition of the parameters refer to Table 2.
The bottom two rows provide numbers from Krautwurst et al. (2025) for the same measurements, but using the cross-sectional flux (CF) method applied separately to the MAMAP2DL / CHARM-F measurements. [2] The value in brackets is the mean flux derived from both instruments obtained with that method, but excluding the two flight legs with the strongest indication for accumulation of CH_4.

Figure 4 shows stacked line profiles of CH_4 enhancements along the flight latitudes, providing an overview of the plume dispersion between 11:20 and 12:40 UTC and of the residual plume over Madrid to the north-west of the sources. The southernmost leg defines the along-wind distance origin. It was flown 1 km upstream of the southern source. As expected, the plume dispersion increases with distance from the sources. Some legs were flown twice; here the CHARM-F measurements show the same variations, except for the noise. The MAMAP2DL enhancements are less noisy and smaller than the CHARM-F enhancements because they are averaged across-track (see Tab. 1) and because they represent the total airmass column between the sun and the detector. The figure corroborates the good match between best-fit model results and observations.

Fit results using only one of the three instruments are shown in Appendix D and the fit results for individual PBL physics schemes are shown in Appendix C.

4 Conclusions

In this paper, we revisit the dataset of Krautwurst et al. (2025), which quantified CH_4 emissions from two Madrid waste sites. We introduce additional in situ measurements recorded during a later flight segment. Compared to the remote-sensing legs, most of these legs are located further downwind of the sources and there are fewer plume crossings in total, making

https://doi.org/10.5194/egusphere-2026-4578
Preprint. Discussion started: 17 August 2026

them less constraining for an independent emission rate estimate. However, by applying a joint transport-model fit analysis method, the in situ measurements provide useful additional input to a combined emission estimate. We therefore produced high-resolution, short-term, local weather simulations using an ensemble of five different PBL schemes to assess transport uncertainties. This method mitigates challenges and uncertainties arising from a highly dynamic wind field, when using the cross-sectional flux method. Nonetheless, very similar results are obtained when removing those measurements that are most affected by accumulation of CH_4.

While both our method and the cross-sectional flux method are viable for the dataset subject to this study, the method presented here can be applied to a wider range of scenarios involving larger scales and extended sources of GHGs. In these scenarios, wind fields need to be tracked over longer distances and periods of time in order to correctly attribute sources and measure emission rates. In addition, as demonstrated through the inclusion of additional in situ measurements, our method offers a flexible way of combining data from different instruments in a single emission rate estimate.

Our approach provides more accurate flux measurements than the cross-sectional flux method, which can provide rapid emission estimates, but relies on assumptions of steady and spatially homogeneous flow. In situations with wind shear, turbulence, or evolving plume dispersion, applying this method leads to large flux errors (e.g. Wolff et al., 2021).

Our method is not targeted at the analysis of longer-term and larger-scale datasets, where oxidation of CH_4 due to OH, or any other feedback and non-linear mechanisms become relevant, due to the pure transport and linear treatment of emission components. It is also not suited for under-constrained problems with a large number of individually modelled source components. For these cases high-dimensional inversion frameworks, such as CTDAS (van der Laan-Luijkx et al., 2017), which optimise fluxes across spatial grids and propagate their error covariances, are better suited. But we demonstrate that this approach poses an efficient and accurate solution for scenarios where the spatial and, as a consequence, also temporal and dynamic dimensions of a multi-component or extended source region do not permit cross-sectional flux measurements.

https://doi.org/10.5194/egusphere-2026-4578
Preprint. Discussion started: 17 August 2026

Appendix A: WRF parametrisation options

In addition to the PBL schemes, the following physical parametrisation options are used. For radiation, we apply the Rapid Radiative Transfer Model scheme for both longwave and shortwave radiation ($ra\_lw\_physics = ra\_sw\_physics = 4$, Iacono et al., 2008). The Morrison two-moment scheme is selected for microphysics ($mp\_physics = 10$, Morrison et al., 2009). For cumulus parametrisation, we use the Grell 3D Ensemble Scheme ($cu\_physics = 5$, Grell and Dévényi, 2002) in the outer domain. The land surface processes are modelled using the Unified Noah land-surface model ($sf\_surface\_physics = 2$, Tewari et al., 2004), which calculates friction velocities and exchange coefficients based on the surface layer scheme. For horizontal diffusion, we use simple diffusion ($diff\_opt = 1$), and for horizontal eddy viscosity, the Smagorinsky first-order closure ($km\_opt = 4$, Smagorinsky, 1963).

Appendix B: Validation of WRF wind with measurements

The flight segment within the PBL took place between approximately 12:50 and 13:35 UTC. Measurements of basic flight and meteorological parameters obtained from the HALO BAHAMAS sensor suite during this period are used to validate the results of the WRF model, particularly with regard to wind speed and direction. Figure B1 compares wind speed and direction from both, the BAHAMAS system and WRF evaluated at the nearest available grid point in latitude, longitude, altitude and time. This includes the time shift identified by the fit. This comparison is, of course, only a snapshot and is hardly representative for the entire wind field within the relevant spatial and temporal bounds, but it can help to identify major discrepancies between the measurements and the simulations. Apart from different noise/turbulence, all WRF runs exhibit small systematic offsets of $\approx 1\,\mathrm{m\,s^{-1}}$ in wind speed and $\approx 10°$ in direction. These discrepancies can probably be explained by a strong gradient in wind speed and direction, right at about the flight altitude of HALO during the in situ measurements (Krautwurst et al., 2025, Appendix D).

Appendix C: Fit results with the individual PBL-physics schemes

The following tables summarise the results of the individual fits of transport models that were performed with different PBL-physics schemes in WRF. For the final result of this study, those were averaged and the scatter interpreted as an estimator for the transport-induced uncertainty to the emission rates. The WRF internal numbering (see Table 5) of PBL schemes is used in the tables below.

Appendix D: Fit using only single instruments

The fit can also be performed using data from only one of the three instruments. Results are shown in Tabs. D1, D2, and D3. While the results for CHARM-F and MAMAP2DL differ only within errors, the fit to JIG data alone differs by a larger margin. The emission rate from the Pinto source is much lower and has a large uncertainty, which can be attributed to the fact that

https://doi.org/10.5194/egusphere-2026-4578
Preprint. Discussion started: 17 August 2026

no in situ measurements were carried out between the two sources. The emission rate of the Valdemingómez source and the overall emission rate are much higher than for the remote-sensing instruments. This is because the Valdemingómez scaling factor has to compensate for the lower Pinto emission rate. The higher overall emission rate, in turn, is caused by the WRF simulations predicting lower mole fractions in the residual plume region over Madrid compared to measurements, especially for the first two flight legs (see Fig. 3, bottom panel). This pulls up the fit, resulting in a higher flux estimate.

https://doi.org/10.5194/egusphere-2026-4578
Preprint. Discussion started: 17 August 2026

Data availability. The MAMAP2DL CH4 column anomalies are available from the authors upon request. The CHARM-F observations and the HALO BAHAMAS in situ dataset (including SHARC and JIG) can be directly obtained from the authors or can be downloaded from the HALO database (https://halo-db.pa.op.dlr.de/ongoing_subset/1384, last access: 2 June 2026). The ECMWF ERA5 data can be downloaded from (Hersbach et al., 2023, https://doi.org/10.24381/cds.adbb2d47, last access: 2 June 2026). The publication contains modified Copernicus Atmosphere Monitoring Service (CAMS) information (2023) downloaded from the CAMS Atmosphere Data Store (CAMS, 2023, https://doi.org/10.24381/ed2851d2, last access: 2 June 2026).

Video supplement. An animation of the best-fit simulated column mole fractions from WRF, compared to the CHARM-F measurements, is available at https://doi.org/10.5281/zenodo.21068389 (Fruck and Wolff, 2026).

Author contributions. Deriving the results presented here involved the contributions of a large team of scientists. This includes the development of hardware and software, the planning of the measurement campaign, data analysis and last but not least the preparation of the manuscript including a thorough internal review process.

KG with support from SK and JB designed and built the MAMAP2DL instrument. JB designed and wrote the operating software for MAMAP2DL. AF, MQ, and MW developed the lidar system CHARM-F. MW designed and wrote the retrieval software for CHARM-F data.

SK developed the flight plan together with inputs from SW and MG. MQ and AF operated the CHARM-F system during the flight. OH operated the MAMAP2DL system during the flight. AF is principal investigator of the CoMet 2.0 mission.

SK performed the analysis of the MAMAP2DL data (from measured spectra to final fluxes) and adapted the algorithms accordingly. SW designed the WRF simulation setup. CF performed the analysis and conversion to column anomalies of the CHARM-F data and a preliminary flux estimate from the CHARM-F data. SK then performed the final flux inversion of CHARM-F data. MG processed the JIG and JAS data.

CF, SW, SK and CK wrote the first draft version of the manuscript. All the authors critically assessed the results and corrected and improved the manuscript in an iterative process.

Competing interests. At least one of the (co-)authors serves as editor for the special issue to which this paper belongs.

Disclaimer. Neither the European Commission nor ECMWF is responsible for any use that may be made of the Copernicus information or data it contains.

Publisher's note: Copernicus Publications remains neutral with regard to jurisdictional claims made in the text, published maps, institutional affiliations, or any other geographical representation in this paper. While Copernicus Publications makes every effort to include appropriate place names, the final responsibility lies with the authors.

https://doi.org/10.5194/egusphere-2026-4578
Preprint. Discussion started: 17 August 2026

Acknowledgements. The simulation results were generated using Copernicus Atmosphere Monitoring Service (CAMS) information [2023] downloaded from the CAMS Atmosphere Data Store (ADS) and Copernicus Climate Change Service information [2023] downloaded from the ECMWF Climate Data Store (CDS). This work used resources of the Deutsches Klimarechenzentrum (DKRZ) granted by its Scientific Steering Committee (WLA) under project ID bd1231. The authors thank Dr. Friedemann Reum (DLR) for his valuable comments on the manuscript's draft.

Financial support. HALO flights during the CoMet 2.0 Arctic mission have been supported by the State of Bremen, by the Max Planck Society (MPG), by the German Aerospace Centre (DLR), and the German Research Foundation (Deutsche Forschungsgemeinschaft - DFG) through its priority programme HALO SPP 1294 "High Altitude and Long Range Research Aircraft (HALO)". The DLR part of CoMet 2.0 Arctic was funded by DLR headquarters, e.g. via the internal MABAK project. MAMAP2DL was in part supported by the University of Bremen, by the State of Bremen (APF), DFG (grant no. BO 1731/2-1), and the Federal Ministry for Education and Research (BMBF, grant no. 01LK1701B).

https://doi.org/10.5194/egusphere-2026-4578
Preprint. Discussion started: 17 August 2026

References

Amediek, A., Ehret, G., Fix, A., Wirth, M., Büdenbender, C., Quatrevalet, M., Kiemle, C., and Gerbig, C.: CHARM-F—a new airborne integrated-path differential-absorption lidar for carbon dioxide and methane observations: measurement performance and quantification of strong point source emissions, Applied Optics, 56, 5182, https://doi.org/10.1364/AO.56.005182, 2017.

Banks, R. F., Tiana-Alsina, J., Baldasano, J. M., Rocadenbosch, F., Papayannis, A., Solomos, S., and Tzanis, C. G.: Sensitivity of boundary-layer variables to PBL schemes in the WRF model based on surface meteorological observations, lidar, and radiosondes during the HygrA-CD campaign, Atmospheric Research, 176-177, 185–201, https://doi.org/https://doi.org/10.1016/j.atmosres.2016.02.024, 2016.

Beck, V., Koch, T., Kretschmer, R., Marshall, J., Ahmadov, R., Gerbig, C., Pillai, D., and Heimann, M.: The WRF Greenhouse Gas Model (WRF-GHG), Technical Report 25, Max Planck Institute for Biogeochemistry, https://www.bgc-jena.mpg.de/5363366/tech_report25.pdf, 2011.

Bevington, P. R. and Robinson, D. K.: Data Reduction and Error Analysis for the Physical Sciences, McGraw-Hill, New York, 3rd edn., ISBN 9780072472271, 2003.

Bretherton, C. S. and Park, S.: A New Moist Turbulence Parameterization in the Community Atmosphere Model, Journal of Climate, 22, 3422 – 3448, https://doi.org/10.1175/2008JCLI2556.1, 2009.

CAMS: Global atmospheric concentrations from inversion of surface and GOSAT satellite observations, Copernicus Atmosphere Monitoring Service (CAMS) Atmosphere Data Store (ADS), https://doi.org/10.24381/ed2851d2, authors: Arjo Segers (TNO), Sander Houweling (VU), institutions: TNO, Utrecht, The Netherlands; Vrije Universiteit, Amsterdam, The Netherlands, last accessed: 2024-10-04, v22r2, 2023.

Crippa, M., Guizzardi, D., Schaaf, E., Monforti-Ferrario, F., Quadrelli, R., Risquez Martin, A., Rossi, S., Vignati, E., Muntean, M., Brandao De Melo, J., Oom, D., Pagani, F., Banja, M., Taghavi-Moharamli, P., Köykkä, J., Grassi, G., Branco, A., and San-Miguel, J.: GHG emissions of all world countries – 2023, Publications Office of the European Union, https://doi.org/doi/10.2760/953322, 2023.

Dembinski, H., Ongmongkolkul, P., Deil, C., Schreiner, H., Feickert, M., Burr, C., Watson, J., Rost, F., Pearce, A., Geiger, L., Abdelmotteleb, A., Desai, A., Wiedemann, B. M., Gohlke, C., Sanders, J., Drotleff, J., Eschle, J., Neste, L., Gorelli, M. E., Baak, M., Eliachevitch, M., and Zapata, O.: scikit-hep/iminuit, https://doi.org/10.5281/zenodo.3949207, 2020.

Díaz-Isaac, L. I., Lauvaux, T., Bocquet, M., and Davis, K. J.: Calibration of a multi-physics ensemble for estimating the uncertainty of a greenhouse gas atmospheric transport model, Atmospheric Chemistry and Physics, 19, 5695–5718, https://doi.org/10.5194/acp-19-5695-2019, 2019.

Domínguez-Sáez, A., Palacios, M. L., Núñez, M. L., and Pujadas, M.: Detection and quantification of large fugitive methane emissions in the Madrid region using ambient concentration measurements and dispersion modeling, Atmospheric Environment, 373, 121 931, https://doi.org/https://doi.org/10.1016/j.atmosenv.2026.121931, 2026.

Ehret, G., Kiemle, C., Wirth, M., Amediek, A., Fix, A., and Houweling, S.: Space-borne remote sensing of CO_2, CH_4, and N_2O by integrated path differential absorption lidar: a sensitivity analysis, Applied Physics B, 90, 593–608, https://doi.org/10.1007/s00340-007-2892-3, 2008.

ESA: European Space Agency: Satellites detect large methane emissions from Madrid landfills, ESA web story, available at https://www.esa.int/Applications/Observing_the_Earth/Satellites_detect_large_methane_emissions_from_Madrid_landfills, last access: 01.06.2026, 2021.

https://doi.org/10.5194/egusphere-2026-4578
Preprint. Discussion started: 17 August 2026

Filges, A., Gerbig, C., Chen, H., Franke, H., Klaus, C., and Jordan, A.: The IAGOS-core greenhouse gas package: a measurement system for continuous airborne observations of CO2, CH4, H2O and CO, Tellus B: Chemical and Physical Meteorology, 67, 27 989, https://doi.org/10.3402/tellusb.v67.27989, 2015.

Fruck, C. and Wolff, S.: WRF-simulated CH4 plume evolution over Madrid waste sites for five PBL schemes, 4 August 2022, https://doi.org/10.5281/zenodo.21068389, 2026.

Gałkowski, M., Jordan, A., Rothe, M., Marshall, J., Koch, F.-T., Chen, J., Agusti-Panareda, A., Fix, A., and Gerbig, C.: In situ observations of greenhouse gases over Europe during the CoMet 1.0 campaign aboard the HALO aircraft, Atmospheric Measurement Techniques, 14, 1525–1544, https://doi.org/10.5194/amt-14-1525-2021, 2021.

Giez, A., Zöger, M., Mallaun, C., Nenakhov, V., Schimpf, M., Grad, C., Numberger, A., and Raynor, K.: Determination of the Measurement Errors for the HALO Basic Data System BAHAMAS by Means of Error Propagation, Tech. rep., DLR-Forschungsbericht, ISSN 1434-8454, https://doi.org/10.57676/5rdc-q708, dLR-FB-2022-27, 2023.

Global Methane Pledge: https://www.globalmethanepledge.org/, (Accessed on 06-07-2025), 2024.

Grell, G. A. and Dévényi, D.: A generalized approach to parameterizing convection combining ensemble and data assimilation techniques, Geophysical Research Letters, 29, 38–1–38–4, https://doi.org/https://doi.org/10.1029/2002GL015311, 2002.

Gunwani, P. and Mohan, M.: Sensitivity of WRF model estimates to various PBL parameterizations in different climatic zones over India, Atmospheric Research, 194, 43–65, https://doi.org/https://doi.org/10.1016/j.atmosres.2017.04.026, 2017.

Hersbach, H., Bell, B., Berrisford, P., Hirahara, S., Horányi, A., Muñoz-Sabater, J., Nicolas, J., Peubey, C., Radu, R., Schepers, D., Simmons, A., Soci, C., Abdalla, S., Abellan, X., Balsamo, G., Bechtold, P., Biavati, G., Bidlot, J., Bonavita, M., De Chiara, G., Dahlgren, P., Dee, D., Diamantakis, M., Dragani, R., Flemming, J., Forbes, R., Fuentes, M., Geer, A., Haimberger, L., Healy, S., Hogan, R. J., Hólm, E., Janisková, M., Keeley, S., Laloyaux, P., Lopez, P., Lupu, C., Radnoti, G., de Rosnay, P., Rozum, I., Vamborg, F., Villaume, S., and Thépaut, J.-N.: The ERA5 global reanalysis, Quarterly Journal of the Royal Meteorological Society, 146, 1999–2049, https://doi.org/https://doi.org/10.1002/qj.3803, 2020.

Hersbach, H., Bell, B., Berrisford, P., Biavati, G., Horányi, A., Muñoz Sabater, J., Nicolas, J., Peubey, C., Radu, R., Rozum, I., Schepers, D., Simmons, A., Soci, C., Dee, D., and Thépaut, J.-N.: ERA5 hourly data on single levels from 1940 to present, Copernicus Climate Change Service (C3S) Climate Data Store (CDS), https://doi.org/https://doi.org/10.24381/cds.adbb2d47, (Accessed on 06-02-2023), 2023.

Hong, S.-Y., Noh, Y., and Dudhia, J.: A New Vertical Diffusion Package with an Explicit Treatment of Entrainment Processes, Monthly Weather Review, 134, 2318 – 2341, https://doi.org/10.1175/MWR3199.1, 2006.

Iacono, M. J., Delamere, J. S., Mlawer, E. J., Shephard, M. W., Clough, S. A., and Collins, W. D.: Radiative forcing by long-lived greenhouse gases: Calculations with the AER radiative transfer models, Journal of Geophysical Research: Atmospheres, 113, https://doi.org/https://doi.org/10.1029/2008JD009944, 2008.

IPCC: Climate Change 2021 – The Physical Science Basis: Working Group I Contribution to the Sixth Assessment Report of the Intergovernmental Panel on Climate Change, https://doi.org/https://doi.org/10.1017/9781009157896, (Accessed on 10-07-2025), 2023.

James, F. and Roos, M.: Minuit - a system for function minimization and analysis of the parameter errors and correlations, Computer Physics Communications, 10, 343–367, https://doi.org/10.1016/0010-4655(75)90039-9, 1975.

Janjić, Z. I.: The Step-Mountain Eta Coordinate Model: Further Developments of the Convection, Viscous Sublayer, and Turbulence Closure Schemes, Monthly Weather Review, 122, 927 – 945, https://doi.org/10.1175/1520-0493(1994)122<0927:TSMECM>2.0.CO;2, 1994.

Jiménez, P. A., Dudhia, J., González-Rouco, J. F., Navarro, J., Montávez, J. P., and García-Bustamante, E.: A Revised Scheme for the WRF Surface Layer Formulation, Monthly Weather Review, 140, 898 – 918, https://doi.org/10.1175/MWR-D-11-00056.1, 2012.

https://doi.org/10.5194/egusphere-2026-4578
Preprint. Discussion started: 17 August 2026

Krautwurst, S., Fruck, C., Wolff, S., Borchardt, J., Huhs, O., Gerilowski, K., Gałkowski, M., Kiemle, C., Quatrevalet, M., Wirth, M., Mallaun, C., Burrows, J. P., Gerbig, C., Fix, A., Bösch, H., and Bovensmann, H.: Identification and quantification of CH_4 emissions from Madrid landfills using airborne imaging spectrometry and greenhouse gas lidar, Atmospheric Chemistry and Physics, 25, 14 669–14 702, https://doi.org/10.5194/acp-25-14669-2025, 2025.

Lauvaux, T. and Davis, K. J.: Planetary boundary layer errors in mesoscale inversions of column-integrated CO2 measurements, Journal of Geophysical Research: Atmospheres, 119, 490–508, https://doi.org/https://doi.org/10.1002/2013JD020175, 2014.

Lucas, D. D., Simpson, M., Cameron-Smith, P., and Baskett, R. L.: Bayesian inverse modeling of the atmospheric transport and emissions of a controlled tracer release from a nuclear power plant, Atmospheric Chemistry and Physics, 17, 13 521–13 543, https://doi.org/10.5194/acp-17-13521-2017, 2017.

Morrison, H., Thompson, G., and Tatarskii, V.: Impact of Cloud Microphysics on the Development of Trailing Stratiform Precipitation in a Simulated Squall Line: Comparison of One- and Two-Moment Schemes, Monthly Weather Review, 137, 991 – 1007, https://doi.org/10.1175/2008MWR2556.1, 2009.

Nakanishi, M. and Niino, H.: Development of an Improved Turbulence Closure Model for the Atmospheric Boundary Layer, Journal of the Meteorological Society of Japan. Ser. II, 87, 895–912, https://doi.org/10.2151/jmsj.87.895, 2009.

Shin, H. H. and Hong, S.-Y.: Representation of the Subgrid-Scale Turbulent Transport in Convective Boundary Layers at Gray-Zone Resolutions, Monthly Weather Review, 143, 250 – 271, https://doi.org/10.1175/MWR-D-14-00116.1, 2015.

Skamarock, W. C., Klemp, J. B., Dudhia, J., Gill, D. O., Liu, Z., Berner, J., Wang, W., Powers, J. G., Duda, M. G., Barker, D. M., and Huang, X.-Y.: A description of the advanced research WRF model version 4, University Corporation for Atmospheric Research, https://doi.org/10.5065/1dfh-6p97, technical Note NCAR/TN-556+STR, 2019.

Smagorinsky, J.: GENERAL CIRCULATION EXPERIMENTS WITH THE PRIMITIVE EQUATIONS: I. THE BASIC EXPERIMENT, Monthly Weather Review, 91, 99 – 164, https://doi.org/10.1175/1520-0493(1963)091<0099:GCEWTP>2.3.CO;2, 1963.

Tewari, M., Chen, F., Wang, W., Dudhia, J., LeMone, M. A., Mitchell, K., Ek, M., Gayno, G., Wegiel, J., , and Cuenca, R. H.: Implementation and verification of the unified NOAH land surface model in the WRF model, 20th conference on weather analysis and forecasting/16th conference on numerical weather prediction, 10–14 January 2004, 14.2a, 2165–2170, https://ams.confex.com/ams/84Annual/webprogram/Paper69061.html, last access: 16 May 2024, 2004.

Tu, Q., Hase, F., Schneider, M., García, O., Blumenstock, T., Borsdorff, T., Frey, M., Khosrawi, F., Lorente, A., Alberti, C., Bustos, J. J., Butz, A., Carreño, V., Cuevas, E., Curcoll, R., Diekmann, C. J., Dubravica, D., Ertl, B., Estruch, C., León-Luis, S. F., Marrero, C., Morgui, J.-A., Ramos, R., Scharun, C., Schneider, C., Sepúlveda, E., Toledano, C., and Torres, C.: Quantification of CH_4 emissions from waste disposal sites near the city of Madrid using ground- and space-based observations of COCCON, TROPOMI and IASI, Atmospheric Chemistry and Physics, 22, 295–317, https://doi.org/10.5194/acp-22-295-2022, 2022.

UNEP: UN Environment Program, Climate and Clean Air Coalition, https://www.ccacoalition.org/, (Accessed on 06-07-2025), 2025.

van der Laan-Luijkx, I. T., van der Velde, I. R., van der Veen, E., Tsuruta, A., Stanislawska, K., Babenhauserheide, A., Zhang, H. F., Liu, Y., He, W., Chen, H., Masarie, K. A., Krol, M. C., and Peters, W.: The CarbonTracker Data Assimilation Shell (CTDAS) v1.0: implementation and global carbon balance 2001–2015, Geoscientific Model Development, 10, 2785–2800, https://doi.org/10.5194/gmd-10-2785-2017, 2017.

Wolff, S., Ehret, G., Kiemle, C., Amediek, A., Quatrevalet, M., Wirth, M., and Fix, A.: Determination of the emission rates of CO2 point sources with airborne lidar, Atmospheric Measurement Techniques, 14, 2717–2736, https://doi.org/10.5194/amt-14-2717-2021, 2021.

https://doi.org/10.5194/egusphere-2026-4578
Preprint. Discussion started: 17 August 2026

Ye, X., Lauvaux, T., Kort, E. A., Oda, T., Feng, S., Lin, J. C., Yang, E. G., and Wu, D.: Constraining Fossil Fuel CO2 Emissions From Urban Area Using OCO-2 Observations of Total Column CO2, Journal of Geophysical Research: Atmospheres, 125, e2019JD030 528, https://doi.org/https://doi.org/10.1029/2019JD030528, 2020.

Yver, C. E., Graven, H. D., Lucas, D. D., Cameron-Smith, P. J., Keeling, R. F., and Weiss, R. F.: Evaluating transport in the WRF model along the California coast, Atmospheric Chemistry and Physics, 13, 1837–1852, https://doi.org/10.5194/acp-13-1837-2013, 2013.

https://doi.org/10.5194/egusphere-2026-4578
Preprint. Discussion started: 17 August 2026

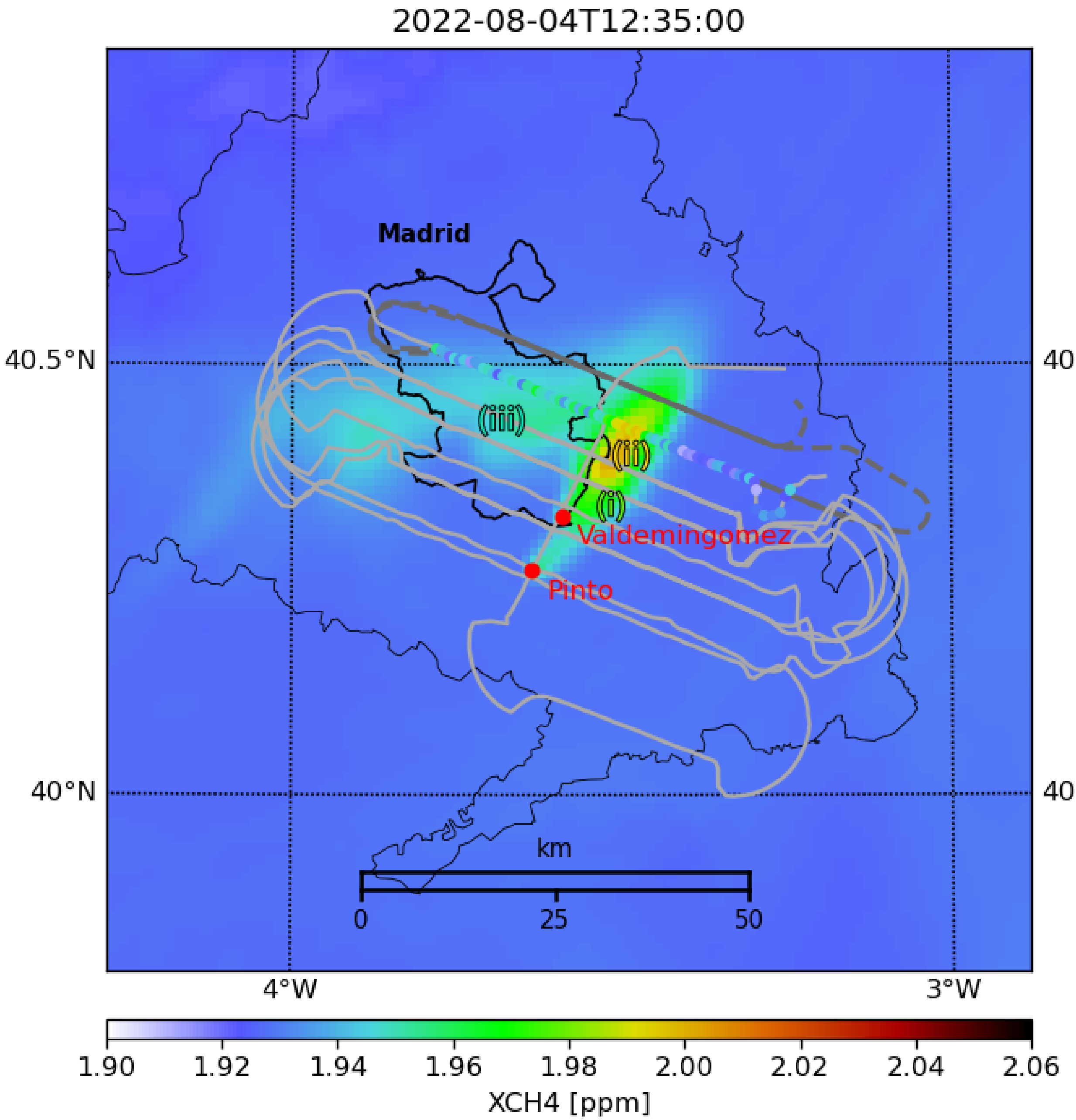

Figure 2. Example of modelled post-fit XCH_4 on the model grid, over the measurement region. CHARM-F measurements coincident in time with the model evaluation are colour-coded along one flight leg. The full remote-sensing and in situ flight patterns are shown in light and dark grey, respectively. The locations of the waste sites are indicated in red. For better geographic orientation, major rivers, region borders, as well as the city of Madrid are highlighted. The plume, an accumulation region within that plume and the residual plume over the city are indicated by (i), (ii) and (iii), respectively.

https://doi.org/10.5194/egusphere-2026-4578
Preprint. Discussion started: 17 August 2026

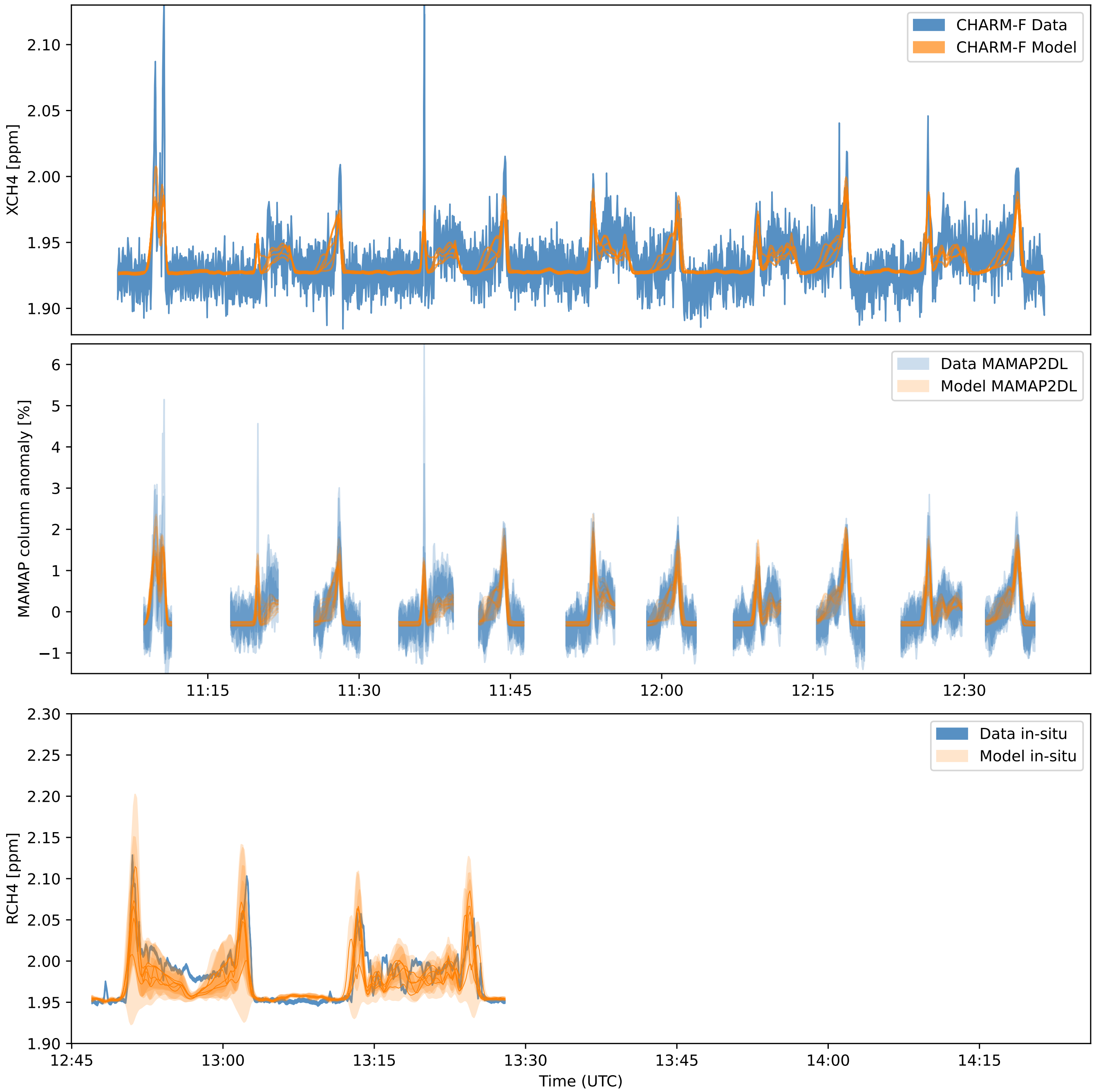

Figure 3. Time series of measurements and post-fit simulations for the three instruments. Results for all five PBL schemes are shown as individual lines. For MAMAP2DL in the central panel all four ground traces along the swath are superposed. The in situ measurements in the bottom panel are later in time, while the top and central panels show the simultaneous remote sensing measurements.

https://doi.org/10.5194/egusphere-2026-4578
Preprint. Discussion started: 17 August 2026

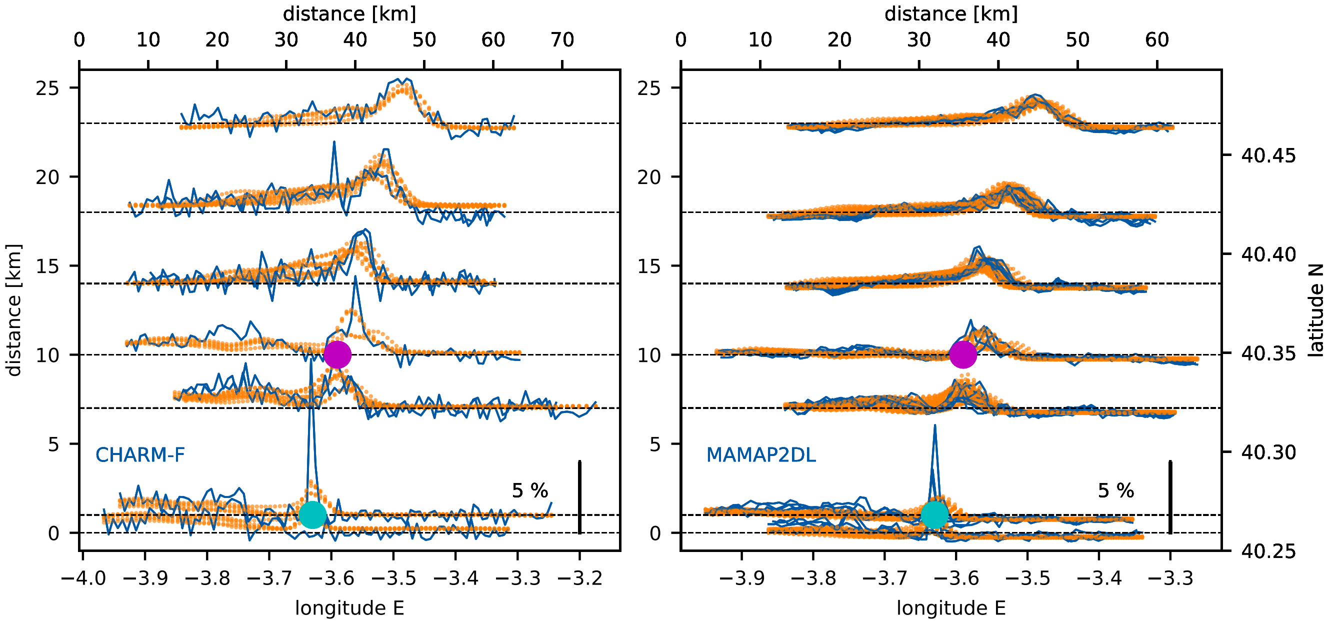

Figure 4. Vertically offset stacked plot of CH_4 enhancement profiles from CHARM-F (left) and MAMAP2DL (right) as a function of longitude. Each transect is displayed as a vertically displaced line plot, with its baseline set to the along-wind distance of the corresponding flight leg (y-axis), such that signal amplitudes represent relative CH_4 enhancements above a locally estimated background. The along-wind distance origin (0 km) corresponds to the southernmost flight leg, upstream of both sources (cyan and purple dots). A 5 % scale bar is provided as enhancement amplitude reference. Enhancements are given in percent above an average background positioned at the corresponding latitude of each flight leg (horizontal lines). All four parallel footprints of MAMAP2DL are superimposed, as well as the fit results of WRF runs with 5 (5×4=20 for MAMAP2DL) different PBL physics schemes (orange). Note that MAMAP2DL measures total column anomalies, whereas CHARM-F measures only the partial column below the aircraft. This results in lower relative enhancements in the MAMAP2DL data, which is also reflected in the simulations.

https://doi.org/10.5194/egusphere-2026-4578
Preprint. Discussion started: 17 August 2026

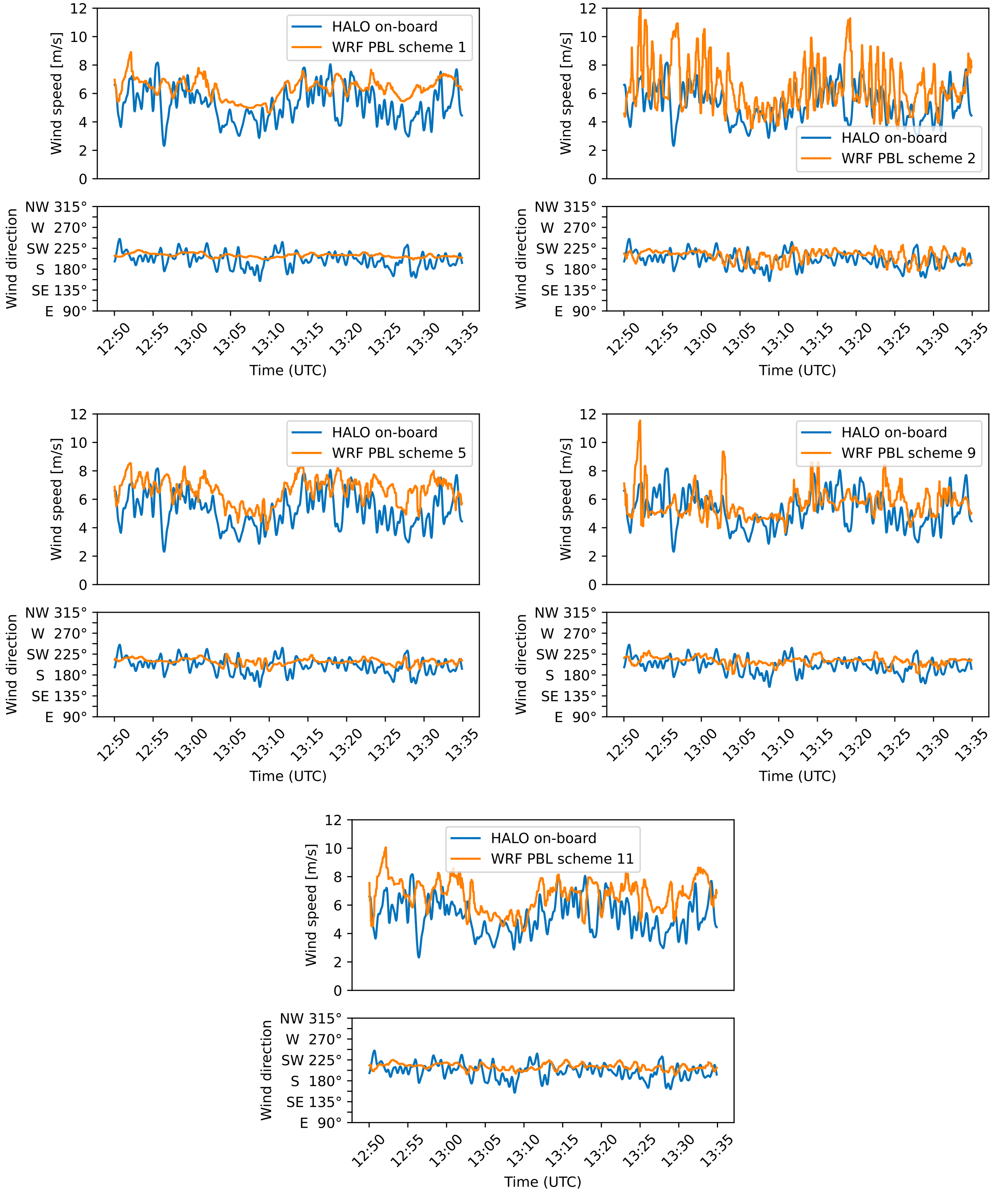

Figure B1. Validation of WRF wind simulations against BAHAMAS measurements for the five PBL physics schemes. The best-fit time shift is applied to the model before comparison.

https://doi.org/10.5194/egusphere-2026-4578
Preprint. Discussion started: 17 August 2026

Table C1. Parameter results of the fit using different PBL schemes.

Scheme	Parameter	Best-fit value	Uncertainty from fit
1	F_{Pinto} [t h^{-1}]	4.506	0.086
	F_{Valde} [t h^{-1}]	5.198	0.093
	Δt [s]	-3409	15
	S_{CAMS}	0.989	0.0015
	S_{IS}	0.997	0.0011
	δ_{CA} [%]	-0.340	0.009
	S_{Pinto}	1.127	0.021
	S_{Valde}	1.040	0.019
2	F_{Pinto} [t h^{-1}]	4.842	0.095
	F_{Valde} [t h^{-1}]	5.038	0.093
	Δt [s]	-2618	10
	S_{CAMS}	0.989	0.0015
	S_{IS}	0.996	0.0012
	δ_{CA} [%]	-0.300	0.009
	S_{Pinto}	1.210	0.024
	S_{Valde}	1.008	0.019
5	F_{Pinto} [t h^{-1}]	1.618	0.053
	F_{Valde} [t h^{-1}]	4.675	0.071
	Δt [s]	-3371	17
	S_{CAMS}	0.990	0.0015
	S_{IS}	0.996	0.012
	δ_{CA} [%]	-0.261	0.009
	S_{Pinto}	0.404	0.013
	S_{Valde}	0.935	0.014
9	F_{Pinto} [t h^{-1}]	4.116	0.085
	F_{Valde} [t h^{-1}]	3.316	0.071
	Δt [s]	-2880	13
	S_{CAMS}	0.990	0.0015
	S_{IS}	0.997	0.011
	δ_{CA} [%]	-0.245	0.008
	S_{Pinto}	1.029	0.021
	S_{Valde}	0.663	0.014
11	F_{Pinto} [t h^{-1}]	4.963	0.092
	F_{Valde} [t h^{-1}]	5.053	0.094
	Δt [s]	-3607	12

https://doi.org/10.5194/egusphere-2026-4578
Preprint. Discussion started: 17 August 2026

Table D1. Fit results using only CHARM-F data.

Parameter	Average result	Std. dev.	Uncert. [%]
$\boldsymbol{F_{\mathrm{Pinto}}\ [\mathrm{t\,h^{-1}}]}$	**4.699**	**1.197**	**25**
$\boldsymbol{F_{\mathrm{Valde}}\ [\mathrm{t\,h^{-1}}]}$	**4.810**	**0.665**	**14**
$\boldsymbol{F_{\mathrm{Total}}\ [\mathrm{t\,h^{-1}}]}$	**9.510**	**1.573**	**17**
Δt [s]	-2990	197	6.6
S_{CAMS}	0.989	3×10^{-4}	0.03
S_{Pinto}	1.175	0.30	25
S_{Valde}	0.962	0.13	14

Table D2. Fit results using only MAMAP2DL data.

Parameter	Average result	Std. dev.	Uncert. [%]
$\boldsymbol{F_{\mathrm{Pinto}}\ [\mathrm{t\,h^{-1}}]}$	**3.515**	**1.085**	**31**
$\boldsymbol{F_{\mathrm{Valde}}\ [\mathrm{t\,h^{-1}}]}$	**4.220**	**0.504**	**12**
$\boldsymbol{F_{\mathrm{Total}}\ [\mathrm{t\,h^{-1}}]}$	**7.735**	**1.401**	**18**
Δt [s]	-3224	184	5.7
δ_{CA} [%]	-0.260	0.035	14
S_{Pinto}	0.879	0.27	31
S_{Valde}	0.844	0.10	12

Table D3. Fit results using only JIG data.

Parameter	Average result	Std. dev.	Uncert. [%]
$\boldsymbol{F_{\mathrm{Pinto}}\ [\mathrm{t\,h^{-1}}]}$	**2.995**	**1.490**	**50**
$\boldsymbol{F_{\mathrm{Valde}}\ [\mathrm{t\,h^{-1}}]}$	**12.659**	**1.681**	**13**
$\boldsymbol{F_{\mathrm{Total}}\ [\mathrm{t\,h^{-1}}]}$	**15.654**	**0.589**	**4**
Δt [s]	-3223	468	15
S_{IS}	0.996	4×10^{-4}	0.04
S_{Pinto}	0.749	0.37	50
S_{Valde}	2.532	0.34	13